

Soft Matter

Accepted Manuscript



This is an *Accepted Manuscript*, which has been through the Royal Society of Chemistry peer review process and has been accepted for publication.

Accepted Manuscripts are published online shortly after acceptance, before technical editing, formatting and proof reading. Using this free service, authors can make their results available to the community, in citable form, before we publish the edited article. We will replace this *Accepted Manuscript* with the edited and formatted *Advance Article* as soon as it is available.

You can find more information about *Accepted Manuscripts* in the [Information for Authors](#).

Please note that technical editing may introduce minor changes to the text and/or graphics, which may alter content. The journal's standard [Terms & Conditions](#) and the [Ethical guidelines](#) still apply. In no event shall the Royal Society of Chemistry be held responsible for any errors or omissions in this *Accepted Manuscript* or any consequences arising from the use of any information it contains.

Understanding geometric instabilities in thin films via a multi-layer model

Emma Lejeune,^a Ali Javili,^a and Christian Linder^{a,*}

Received October 15, 2015

When a thin stiff film adhered to a compliant substrate is subject to compressive stresses, the film will experience a geometric instability and buckle out of plane. For high film/substrate stiffness ratios with relatively low levels of strain, the primary mode of instability will either be wrinkling or buckling delamination depending on the material and geometric properties of the system. Previous works approach these systems by treating the film and substrate as homogenous layers, either consistently perfectly attached, or perfectly unattached at interfacial flaws. However, this approach neglects systems where the film and substrate are uniformly weakly attached or where interfacial layers due to surface modifications in either the film or substrate are present. Here we demonstrate a method for accounting for these additional thin surface layers via an analytical solution verified by numerical results. The main outcome of this work is an improved understanding of how these layers influence global behavior. We demonstrate the utility of our model with applications ranging from buckling based metrology in ultrathin films, to an improved understanding of the formation of a novel surface in carbon nanotube bio-interface films. Moving forward, this model can be used to interpret experimental results, particularly for systems which deviate from traditional behavior, and aid in the evaluation and design of future film/substrate systems.

1 Introduction

Understanding geometric instability behavior in stiff films with nanoscale thickness adhered to compliant substrates is increasingly important for engineering novel systems.¹ In these thin films, the contribution of inhomogeneities due to interfacial regions with finite thickness cannot be ignored.² Therefore, we are lead to the questions: how can these additional interfacial layers be accounted for? And, how can considering these layers enhance our understanding of geometric instabilities in novel engineered systems? We approach these questions by introducing a multi-layer model with an analytical solution verified by numerical results. Then, we apply our model to previous experimental research in buckling based metrology in ultrathin films^{3–5} and topology formation in carbon nanotube bio-interface film morphologies.⁶

In general, potential sources of compressive stress that can result in geometric instability are mechanical loading, confined thermal loading, and confined or differential material growth and swelling.^{7,8} Though many other types of geometric instability exist,⁹ and their understanding may be enhanced by the inclusion

of interfacial layers, we limit the scope of our paper to systems that will primarily experience wrinkling and buckling delamination, which is reasonable for thin stiff films adhered to compliant substrates under relatively low levels of compression.¹⁰ In

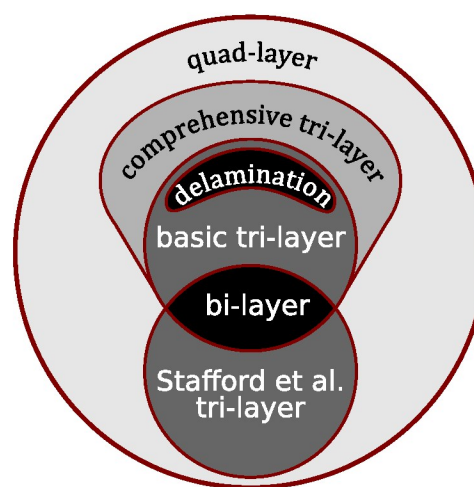


Fig. 1 This image summarizes all of the multi-layer models for approaching thin films with interfacial layers that are covered in depth in this paper. Our contributions are the basic tri-layer model, the comprehensive tri-layer model and the quad-layer model, which unifies everything pictured. Table 1 illustrates each model and summarizes the equations necessary for implementation

^a Department of Civil and Environmental Engineering, Stanford University, Stanford, CA 94305, USA

* Corresponding author. Electronic mail: linder@stanford.edu

studying wrinkling, Biot¹¹ originally proposed an analytical solution to the wrinkling instability, which has subsequently been demonstrated in experimental systems,¹² while buckling delamination has also been studied extensively.¹³ In general, controlling these instabilities is a desired outcome because their effects can range from highly beneficial to destructive. Instabilities are beneficial in applications such as biological pattern formation, flexible electronics, buckling based metrology and controlling surface topological features.^{8,14–24} However, these instabilities also trigger global and local failure in multi-layer systems,^{25,26} whose numerical approximation through the finite element method is challenging.^{27–30}

The conditions under which buckle delamination or wrinkling occur have been well studied using numerical and analytical solutions that capture one instability mode at a time.^{31–34} In determining which instability will occur, a standard approach is to assume an initial flaw size (required to initiate buckling delamination) and compare the point of instability initiation for both modes given a set of material parameters.¹⁰ Recent research has covered instabilities in specific complex systems, such as graphene layers,³⁵ systems which utilize surface patterning³⁶ and semiflexible polymer networks,³⁷ multiphysics effects,³⁸ and more complex versions of instability initiation and post buckling behavior beyond the scope of simple wrinkling and buckling delamination.^{39–42} With regard to buckling instabilities of layered films, interfacial layers have been accounted for by calculating the total contribution to film stiffness as layers in a composite plate,^{4,43–45} and by combining the interfacial layer with the substrate.⁴⁶ In Fig. 1 we illustrate an overview of our contribution to modeling thin films with interfacial regions.

The rest of the paper is organized as follows. Section 2 describes the multi-layer model that we propose to explain instabilities and summarizes previous work that is recovered by our model. Section 3 describes multiple applications of our model, ranging from buckling metrology to novel devices, and concluding remarks are given in Section 4.

2 Multi-layer model

Wrinkling behavior of a thin layer on a compliant substrate under compression is typically explained by the well-established bi-layer model.^{11,47,48} In this model, the substrate is assumed to be an infinite half-space and the media on top of the substrate is treated as a film perfectly bonded to the substrate. The wrinkling behavior is characterized by a sinusoidal wave, with wavelength at instability initiation λ_{cr} determined by the material and geometric properties of the system. We propose a more sophisticated model designed to explain the wrinkling behavior of systems with thin interfacial layers. To accomplish this, we treat the medium on top of the substrate as three layers, namely, an intermediate layer, a film layer and a top layer, hence a multi-layer model.

In the first model that we propose in this section, the basic tri-layer model, the intermediate layer between the film and the substrate represents the bonding interface between the two media. Next, we detail the approach taken in Stafford *et al.*,⁴ where a top interfacial layer is introduced specifically to capture the surface softening behavior of ultrathin amorphous polymer films. In-

spired by this, we propose a comprehensive tri-layer model which extends the range of interfacial stiffness captured by our basic tri-layer model. Finally, our proposed quad-layer model, detailed in Sec. 2.4, is a combination of our own comprehensive tri-layer model and the Stafford *et al.* tri-layer model. The remainder of this section details multiple configurations of film and interfacial layers, all of which are summarized succinctly with the equations necessary for implementation in Table 1.

In passing, we mention that recently Jia *et al.*⁴⁶ studied the buckling behavior of a bi-layer film on a compliant substrate where depending on material and geometric properties, distinguishable families of wrinkling solutions are possible. One important feature of our model is that, motivated by the applications that we have in mind, the thicknesses of the layers compared to the film thickness are fairly small. This contrasts with the work of Jia *et al.*⁴⁶, where their main contribution is an analytical solution for the case where an additional included intermediate layer is generally thicker than the film, and, roughly speaking, serves as a modification to the substrate.

2.1 Basic tri-layer model

Our proposed basic tri-layer model, Fig. 2 considers an attachment region in addition to the film and substrate layers therefore changing the fundamental behavior of the system. Physically, an intermediate layer arises either intentionally, or as a consequence of the manufacturing process that causes an intermediate region with material parameters that are different from the film and substrate.^{49–51} It is important to acknowledge the presence of these layers because an intermediate region can alter global system behavior and could create unintentional or unexplained consequences such as premature instability initiation or an unpredicted buckled shape. In our model, an intermediate layer stiffness approaching zero physically corresponds to a film and substrate that are not attached, and recovers a buckling delamination instability mode. An intermediate layer that is as stiff as the substrate layer corresponds to perfect attachment between the film and substrate, and recovers the wrinkling instability mode. Our model is primarily intended to access what occurs between these two extremes, specifically an intermediate layer stiffness corresponding to imperfect attachment, which will provide physical insight to instability behavior that is not already well understood.

Our analytical solution for instability initiation in the tri-layer system is based on a modification of the well studied wrinkling instability in bi-layer systems.⁴⁷ In our modified system, the strain in the film, ϵ , is obtained as

$$\epsilon = \frac{1}{12} t_f^2 n^2 + \frac{2E_s}{E_f t_f} \frac{1}{\zeta n + 2t_i [E_s/E_i - 1] n^2}. \quad (1)$$

The parameters E_f , E_i , E_s , are the plane strain elastic moduli for the film, intermediate layer and substrate and t_f , t_i , and t_s are the thickness of the film, intermediate layer and substrate respectively. The constant ζ is a function of Poisson's ratio of the substrate, $\zeta = [3 - 4\nu_s]/[1 - \nu_s]^2$, and n is the wave number of the folding pattern of the film.

In order to derive (1), we introduce the concept of effective

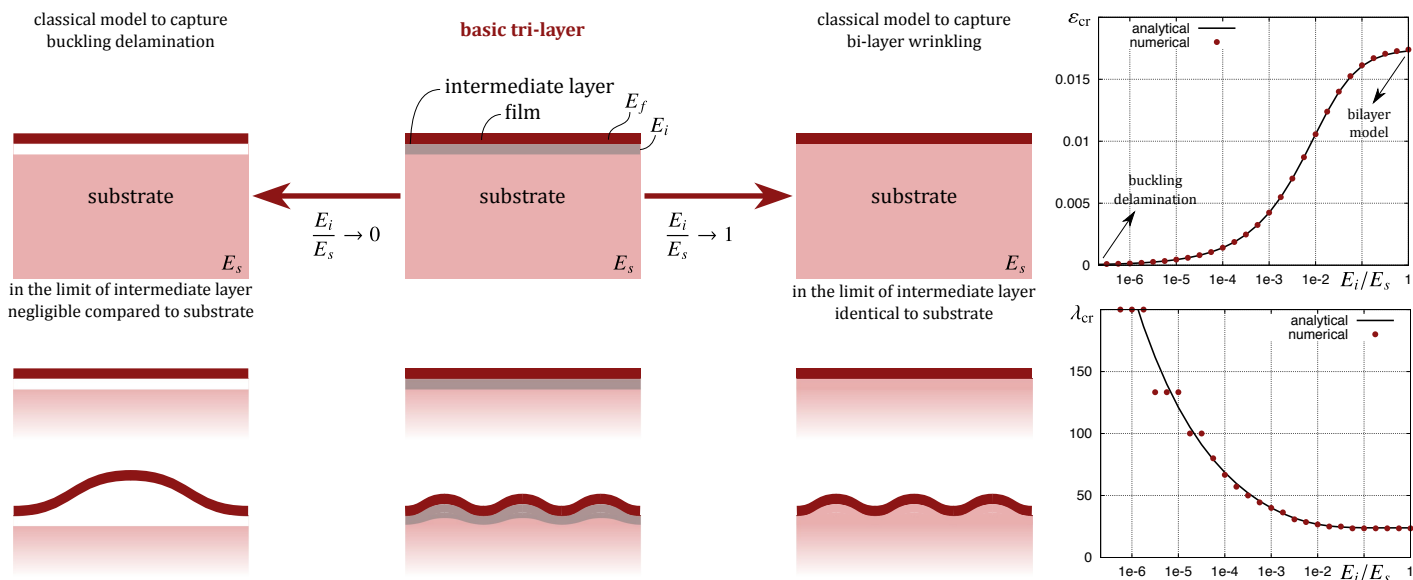


Fig. 2 Left: Summary of how our tri-layer model fits into the existing framework for understanding the behavior of thin films on compliant elastic substrates. Unlike buckling delamination (column 1), assuming perfect detachment, and unlike bi-layer wrinkling (column 3), assuming perfect attachment, our basic tri-layer model (column 2) allows for the case of imperfect attachment between the film and the substrate. The intermediate layer stiffness ranges from 0, perfect detachment, to E_s , perfect attachment. The second and third row show the undeformed configuration and folding patterns due to applied compression, respectively. Upper right: Critical strain ϵ_{cr} with respect to intermediate layer stiffness (presented as the ratio between E_i and E_s). Lower right: Critical wavelength λ_{cr} with respect to intermediate layer stiffness. In these plots, the length scale is defined by the thickness of the film and intermediate layer. For this example, we assign $t_f = 1 \text{ nm}$, $t_i = 0.1 \text{ nm}$ and $E_f = 200E_s$. Therefore, λ_{cr} is reported in nm .

stiffness assuming that the intermediate layer represents a set of parallel springs between the film and the substrate. The effective stiffness of the substrate and the intermediate layer are $K_s = E_s/t_s$ and $K_i = E_i/t_i$, respectively. Note that the substrate is assumed to be an infinite half-space and hence, t_s shall be understood as an unknown parameter to represent the substrate stiffness. First, the combination of intermediate layer and substrate is treated as the combination of springs in series, and therefore the total effective stiffness of the substrate and the intermediate layer is $K = K_i K_s / [K_i + K_s]$. Second, according to our definition of the effective stiffness, we can write $K = E/[t_s + t_i]$, where E is the combined modulus of the intermediate layer and substrate. Third, using the Airy stress functions and bi-harmonic operator for an infinite half-space, the analytical solution for the total effective stiffness reads $K = 2nE/\zeta$. Therefore, we have three equations and three unknowns, K , t_s , E . Clearly all the unknowns remain a function of the wave number n . The relation (1) is obtained using the standard procedure⁴⁷ for bi-layer system in which we substitute the substrate parameters by the total substrate plus intermediate layer. In the extreme of $E_i = E_s$, (1) is identical to bi-layer systems and in the extreme of $E_i \rightarrow 0$ it reduces to the buckling delamination behavior, as illustrated in Fig. 2. By setting the derivative ϵ with respect to n equal to zero, we can directly determine the critical wave number n_{cr} as the solution to the resulting implicit equation using Newton's method. Then, the value of ϵ_{cr} is the solution to (1) using n_{cr} . We can determine the wavelength at the point of instability initiation, λ_{cr} as $\lambda_{cr} = 2\pi/n_{cr}$. Fig. 2 shows our equations for critical strain and wavelength validated by numerical results obtained using the finite element method.⁵²

2.2 Tri-layer model of Stafford et al.

In this section we briefly describe the tri-layer model proposed in Stafford *et al.*⁴ in which a thin top layer rests at the free surface of the film. The plane strain elastic modulus and thickness of the top layer are denoted E_t and t_t , respectively. In this approach, the film is assumed to be perfectly attached to the substrate and therefore, the effective stiffness of the substrate is identical to that of the bilayer model. However, the effective stiffness of the film and the top layer together is obtained via the rule of mixtures similar to well-established sandwich theory of composite beams. The overall axial and bending stiffness of the film plus the top layer read

$$[Et]_{tot.} = E_f t_f + E_t t_t \quad \text{and} \quad [EI]_{tot.} = E_f I_f + E_t I_t \quad (2)$$

respectively. The moments of inertia of the film and the top layer are denoted I_f and I_t , respectively and can be calculated as

$$I_f = \frac{1}{12} t_f^3 + t_f \left[\frac{t_f}{2} - \bar{y} \right]^2 \quad \text{and} \quad I_t = \frac{1}{12} t_t^3 + t_t \left[t_f + \frac{t_t}{2} - \bar{y} \right]^2 \quad (3)$$

in which \bar{y} denotes the coordinate of the neutral axis. The distance from the bottom of the film where the film meets the substrate can then be obtained as

$$\bar{y} = \frac{\left[\frac{t_f}{2} \right] E_f t_f + \left[t_f + \frac{t_t}{2} \right] E_t t_t}{[Et]_{tot.}} \quad (4)$$

Note, here and henceforth, in calculations of areas and moments of inertia, the width of the layers are neglected as we are dealing with a two dimensional model. This is equivalent to normalizing all the values by the width.

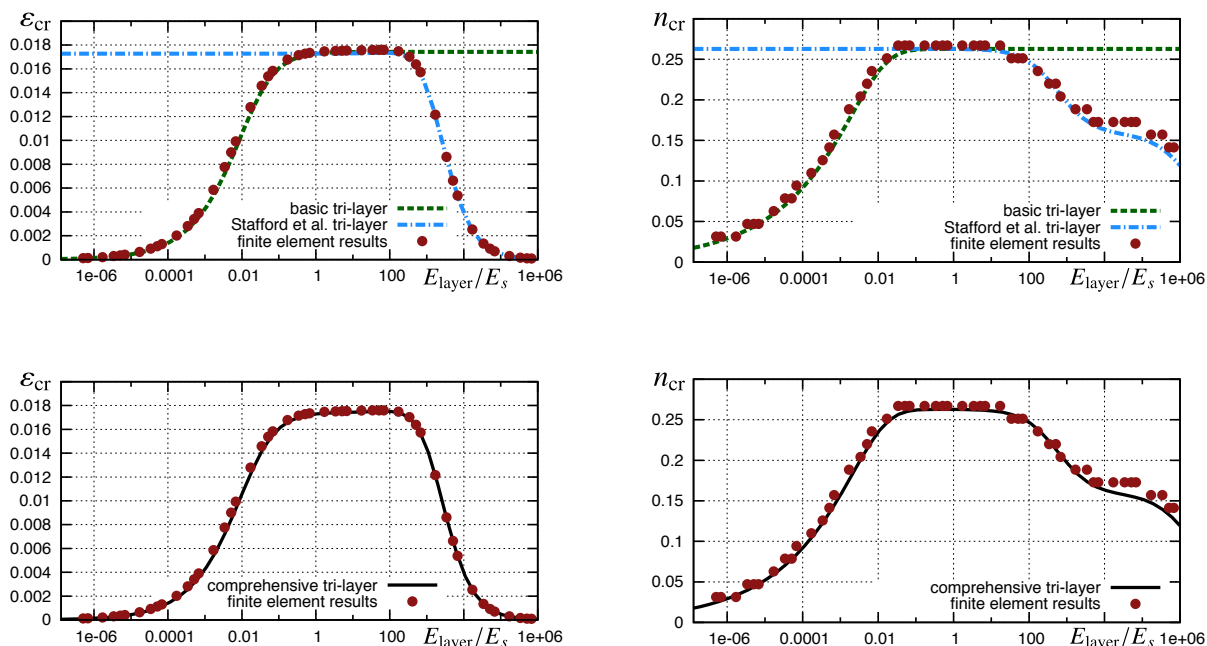


Fig. 3 Comparison of different tri-layer models to capture the critical strain ε_{cr} and the critical wave number n_{cr} . The upper plots illustrate the basic tri-layer model and the Stafford *et al.* tri-layer model. The lower plots illustrate the comprehensive tri-layer model, which is able to capture the entire domain alone. The finite element results correspond to a system where the interfacial layer rests between the film and the substrate. If the layer were to rest on top of the substrate, the Stafford model would capture the full range of intermediate layer stiffness. In these plots, the length scale is defined by the thickness of the film and intermediate layer. For this example, we assign $t_f = 1 \text{ nm}$, $t_i = 0.1 \text{ nm}$ and $E_f = 100E_s$. Therefore, n_{cr} is reported in nm^{-1} .

2.3 Comprehensive tri-layer model

Next, we introduce our comprehensive tri-model by enhancing the intermediate layer in our model proposed in Sec. 2.1 with its own stiffness similar to the approach taken in Sec. 2.2. The effective stiffness of the film and the intermediate layer together read as

$$[Et]_{tot.} = E_i t_i + E_f t_f \quad \text{and} \quad [EI]_{tot.} = E_i I_i + E_f I_f \quad (5)$$

respectively. The moments of inertia of the film and the intermediate layer denoted I_f and I_i , respectively are

$$I_i = \frac{1}{12} t_i^3 + t_i \left[\frac{t_i}{2} - \bar{y} \right]^2 \quad \text{and} \quad I_f = \frac{1}{12} t_f^3 + t_f \left[t_i + \frac{t_f}{2} - \bar{y} \right]^2 \quad (6)$$

in which \bar{y} denotes the distance of the neutral axis from the bottom of the intermediate layer computed as

$$\bar{y} = \frac{\left[\frac{t_i}{2} \right] E_i t_i + \left[t_i + \frac{t_f}{2} \right] E_f t_f}{[Et]_{tot.}} \quad (7)$$

The governing equation for the bending of the layers on the substrate is

$$[EI]_{tot.} w'''' + [EA]_{tot.} \varepsilon w'' = -K w \quad (8)$$

in which, following the methodology of Sec. 2.1, the effective stiffness of the substrate together with the intermediate layer K is a function of the wave number n and proves to be

$$K(n) = \frac{2E_s n}{\zeta + 2t_i [E_s/E_i - 1] n} \quad (9)$$

The general solution of the governing equation (8) is a sinusoidal

wave $w = w_0 \sin(nx)$ and inserting that in to (8), leads to

$$[EI]_{tot.} n^4 - [EA]_{tot.} \varepsilon n^2 = -K \quad (10)$$

which yields an expression for the compressive strain ε as

$$\varepsilon = \frac{[EI]_{tot.}}{[EA]_{tot.}} n^2 + \frac{K}{[EA]_{tot.} n^2} \quad (11)$$

In order to compute the critical wave number and its associated critical strain, we set the derivative of the strain with respect to the wave number n to zero or

$$\frac{\partial \varepsilon}{\partial n} \stackrel{!}{=} 0 \quad \iff \quad n = n_{cr} \quad \text{and} \quad \varepsilon_{cr} = \varepsilon(n_{cr})$$

that is equivalent to solving the equation

$$2[EI]_{tot.} n^4 + K' n - 2K \stackrel{!}{=} 0 \quad (12)$$

where K' denotes the derivative of the effective stiffness K with respect to n as

$$K' = \frac{2E_s \zeta}{[\zeta + 2t_i [E_s/E_i - 1] n]^2} \quad (13)$$

Figure 3 compares the critical strain and wave number n_{cr} for the three tri-layer models presented in Sec. 2.1, 2.2 and 2.3. The horizontal axis shows a wide range for the layer stiffness normalized by the substrate stiffness. Clearly, the layer stiffness corresponds to the top layer in the case of the tri-layer model of Stafford *et al.* and to the intermediate layer in the case of our basic and comprehensive tri-layer models. Also, numerical results using eigenvalue analysis in the finite element method are given corresponding to a tri-layer model with an intermediate layer. It


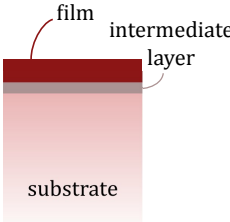
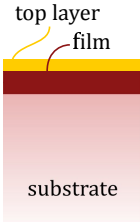
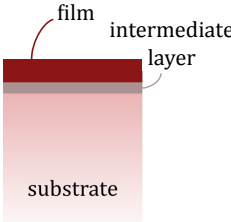
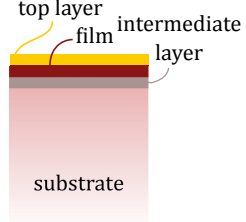
illustration					
model	bi-layer	basic tri-layer	Stafford tri-layer	comprehensive tri-layer	quad-layer
applications	explain the wrinkling behavior of a compressed layer on a compliant substrate	capture the bonding characteristic between the film and the substrate via an intermediate layer	explain the behavior in ultrathin amorphous polymer films via introducing a top layer	capture the bonding between the film and substrate as well as the stiffness of the layer along the film	include the top layer of Stafford et al. (2006) and the intermediate layer of the comprehensive trilayer model
α	$\alpha(t_i = 0, t_t = 0)$ $= E_f I_f$	$\alpha(t_i = 0, t_t = 0)$ $= E_f I_f$	$\alpha(t_i = 0, t_t \neq 0)$ $= E_f I_f + E_t I_t$	$\alpha(t_i \neq 0, t_t = 0)$ $= E_f I_f + E_i I_i$	$\alpha(t_i \neq 0, t_t \neq 0)$ $= E_f I_f + E_t I_t + E_i I_i$
β	$\beta(t_i = 0, t_t = 0)$ $= E_f t_f$	$\beta(t_i = 0, t_t = 0)$ $= E_f t_f$	$\beta(t_i = 0, t_t \neq 0)$ $= E_f t_f + E_t t_t$	$\beta(t_i \neq 0, t_t = 0)$ $= E_f t_f + E_i t_i$	$\beta(t_i \neq 0, t_t \neq 0)$ $= E_f t_f + E_t t_t + E_i t_i$
K	$K(t_i = 0)$ $= \frac{2E_s n}{\zeta}$	$K(t_i \neq 0)$ $= \frac{2E_s n}{\zeta + 2t_i[E_s/E_i - 1]n}$	$K(t_i = 0)$ $= \frac{2E_s n}{\zeta}$	$K(t_i \neq 0)$ $= \frac{2E_s n}{\zeta + 2t_i[E_s/E_i - 1]n}$	$K(t_i \neq 0)$ $= \frac{2E_s n}{\zeta + 2t_i[E_s/E_i - 1]n}$
$\varepsilon = \frac{\alpha}{\beta} n^2 + \frac{K(n)}{\beta n^2} \quad , \quad 2\alpha n_{cr}^4 + K' n_{cr} - 2K \stackrel{!}{=} 0 \quad , \quad \varepsilon_{cr} = \varepsilon(n_{cr})$					
$\alpha = E_i \left[\frac{1}{12} t_i^3 + t_i \left[\frac{t_i}{2} - \frac{[\frac{t_i}{2}] E_i t_i + [t_i + \frac{t_i}{2}] E_f t_f + [t_i + t_f + \frac{t_i}{2}] E_t t_t}{E_i t_i + E_f t_f + E_t t_t} \right]^2 \right]$ $+ E_f \left[\frac{1}{12} t_f^3 + t_f \left[t_i + \frac{t_f}{2} - \frac{[\frac{t_i}{2}] E_i t_i + [t_i + \frac{t_i}{2}] E_f t_f + [t_i + t_f + \frac{t_i}{2}] E_t t_t}{E_i t_i + E_f t_f + E_t t_t} \right]^2 \right]$ $+ E_t \left[\frac{1}{12} t_t^3 + t_t \left[t_i + t_f + \frac{t_t}{2} - \frac{[\frac{t_i}{2}] E_i t_i + [t_i + \frac{t_i}{2}] E_f t_f + [t_i + t_f + \frac{t_i}{2}] E_t t_t}{E_i t_i + E_f t_f + E_t t_t} \right]^2 \right]$ $\beta = E_i t_i + E_f t_f + E_t t_t$ $K = \frac{2E_s n}{\zeta + 2t_i[E_s/E_i - 1]n}$ $K' = \frac{2E_s \zeta}{[\zeta + 2t_i[E_s/E_i - 1]n]^2}$					

Table 1 This table is a summary of each model presented in Section 2. The bi-layer model is the traditional model for capturing the wrinkling instability, and the remainder of the models are adaptations of the bi-layer model to account for interfacial layers. The quad-layer model is a generalized version of all the other models, including the basic tri-layer model and comprehensive tri-layer model, both proposed in this paper, and the Stafford *et al.* model. The parameters α , β are defined for simplicity and correspond to the derivations in Sec. 2. The parameters α , β and K vary based on which model selected but the equations for ε and n_{cr} maintain the same structure. The basic tri-layer model, the comprehensive tri-layer model and the quad-layer model result in implicit equations, while the bi-layer model and the Stafford tri-layer model result in explicit equations.

is clear the basic tri-layer model can very well capture the material response if the intermediate layer is less compliant than the substrate, but breaks down beyond that. The opposite holds

for the Stafford *et al.* tri-layer model, which can be justified by the fact that a compliant top-layer can not substantially influence the overall response. Finally, the comprehensive tri-layer model

shows excellent agreement with the numerical results for the entire range of intermediate layer stiffness for both ϵ_{cr} and n_{cr} .

2.4 Quad-layer model as generalization of current models

The comprehensive tri-layer model furnishes extremely promising results, however, one can argue that this model may not be sufficiently general for capturing all ultrathin film regimes. Specifically, without adjustment the comprehensive tri-layer model will not capture layers at both the top and bottom of the thin film independently, which may be necessary in some cases.^{2,4} This motivates the introduction of a quad-layer model. Our quad-layer model consists of the substrate and three layers on top of it. The film lies between the top layer and the intermediate layer resting on the substrate. The distance of the neutral axis from the bottom of the intermediate layer is denoted \bar{y} is

$$\bar{y} = \frac{\left[\frac{t_i}{2}\right]E_i t_i + \left[t_i + \frac{t_f}{2}\right]E_f t_f + \left[t_i + t_f + \frac{t_i}{2}\right]E_t t_i}{E_i t_i + E_f t_f + E_t t_i}. \quad (14)$$

The overall bending stiffness of the three layers combined reads

$$\begin{aligned} [EI]_{tot.} &= E_i I_i + E_f I_f + E_t I_t \\ &= E_i \left[\frac{1}{12} t_i^3 + t_i \left[\frac{t_i}{2} - \bar{y} \right]^2 \right] \\ &+ E_f \left[\frac{1}{12} t_f^3 + t_f \left[t_i + \frac{t_f}{2} - \bar{y} \right]^2 \right] \\ &+ E_t \left[\frac{1}{12} t_t^3 + t_t \left[t_i + t_f + \frac{t_t}{2} - \bar{y} \right]^2 \right]. \end{aligned} \quad (15)$$

The overall axial stiffness of the three layers is defined as

$$[EA]_{tot.} = E_i t_i + E_f t_f + E_t t_t. \quad (16)$$

The governing equations and relations (8)–(13) hold for the quad-layer, as well.

Equipped with the quad-layer model, one can readily show that the previous models are indeed degenerations of this generalized model. Table 1 gathers all the models and clarifies how the quad-layer model reduces to each, consistent with the generality illustrated in Fig. 1. In Table 1, the first column is the classical bilayer model and is the simplest model to capture instabilities of a film on a compliant substrate. The second, third and fourth columns are the tri-layer models of Sec. 2.1, 2.2 and 2.3, respectively. The last column is the quad-layer model discussed here. Note, the intermediate layer shall be understood as the bonding layer between the film and the substrate and the zero thickness intermediate layer $t_i = 0$ is equivalent to the limit case of perfect attachment between the film and the substrate. Furthermore, for the two cases of the bilayer model and the tri-layer model of Stafford et al. where the film is perfectly attached to the substrate, a closed form analytical solution exist which is not the case in general and the governing equation (12) should be solved using an iterative scheme such as Newton's method.

3 Model applications

Significant applications of the models proposed in Sec. 2 are in buckling based metrology and in the fabrication of novel surfaces and devices. In Sec. 3.1, we apply our model to buckling based metrology of ultrathin films and compare it to the methodology proposed by Stafford *et al.*⁴ In Sec. 3.2, we discuss how our model could be used to understand the surface topology formation observed in Xie *et al.*⁶ and comment on how it could be used to capture instability behavior in embedded thin films.

3.1 Applications in buckling based metrology

Buckling based metrology is an important application of wrinkling behavior in thin films adhered to compliant substrates.^{1,3,22,53,54} For traditional thin film bi-layers, it has been demonstrated that given known or prescribed film thickness and substrate properties, film modulus can be computed directly from the equation

$$E_f = 3E_s \left(\frac{\lambda_{cr}}{2\pi t_f} \right)^3 \quad (17)$$

where λ_{cr} is the experimentally measured wrinkle wavelength.⁴ The typical resulting plot of film thickness vs. wavelength is a straight line through the origin. This is particularly relevant to creating new materials which may be impossible to manufacture in bulk format for traditional stiffness testing. For example, in creating nanocomposites, where modulus is often not previously known, gold bilayer films⁴⁴ and polyelectrolyte bilayer films^{45,55} can be approximated as layered composite beams and studied using buckling based metrology. In contrast, gold nanoparticles embedded in a polystyrene sheet exhibits an effective film layer with a significantly reduced modulus compared to a layered Au-PS composite, which indicates that the Au particles have sufficient gaps between them to produce a unique form of nanocomposite not captured by a layered composite beam.⁵⁶ In addition to these examples of intentional multi-layer films, it has been demonstrated that for films classified as “ultrathin” (thickness under 100 nm), experimental measurements deviate from well understood behavior in a manner that indicates unintentional additional layers may be present. This deviation manifests when plotting thickness vs. wavelength produces a straight line offset from the origin.^{4,5,57–61}

To explain this deviating behavior, it is necessary to account for the presence of finite regions within the thin film that have altered properties. Specifically, a weaker layer near the free surface of a polymer film potentially due to increased chain mobility has been identified as one possible source of this softening and observed via molecular dynamics simulations^{2,62} and experimental particle embedment and nano-indentation testing.^{63,64} A layer with modified surface properties near the film/substrate interface has also been proposed and modeled in molecular dynamics simulations.² Notably, substrate and film surface modifications such as UV exposure or ozone may produce interfacial regions with different stiffness between film and substrate,^{59,65,66} or the upper layer of the substrate may become highly integrated with the film to produce an stiffened interfacial region.⁶⁷ Because the thickness of these altered regions is on the order of 1–10 nm, their effects

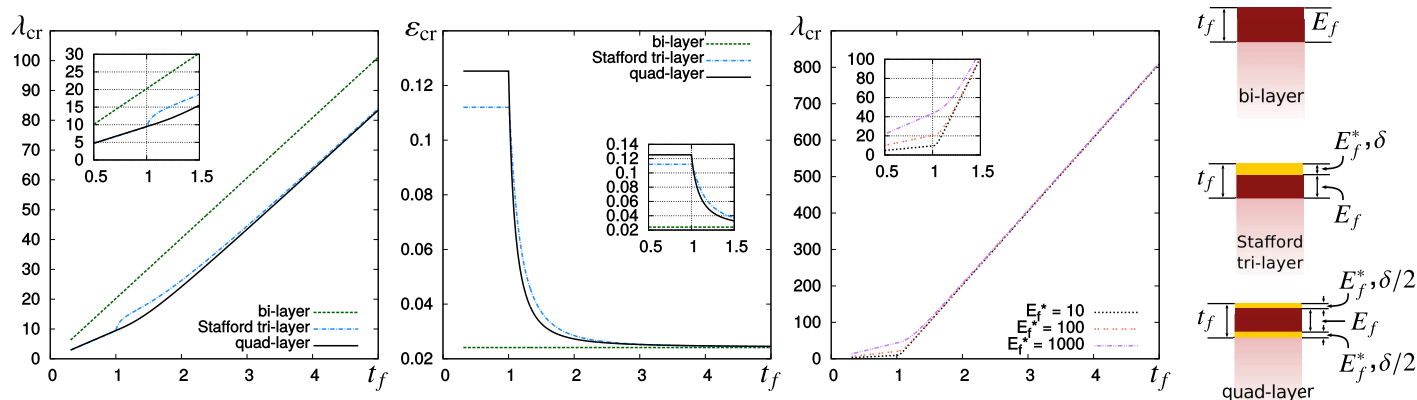


Fig. 4 The left and center plots illustrate the differences between our quad-layer model, the Stafford model and the bi-layer model for n_{cr} and ϵ_{cr} respectively. In these plots, the length scale is defined by t_f and δ . For this example, we vary t_f (nm), set $\delta = 1$ nm, $E_f = 100E_s$ and $E_f^* = 10E_s$. Therefore, λ_{cr} is reported in nm. The right plot illustrates, using our model, how the stiffness of the interfacial layers E_f^* is difficult to quantify without examining data where $t_f \approx \delta$. In this example, we vary t_f (nm), with $E_f = 10^5 E_s$ and E_f^* reported in the legend as a multiples of E_s . Resulting values of λ_{cr} are reported in nm. The schematic drawings are included in order to make clear the notation, originally used in Stafford *et al.*, and subsequently used in this section of our paper.

Source	Reported E_f (GPa)	Reported E_f^* (GPa)	Reported δ (nm)	Proposed E_f (GPa)	Proposed E_f^* (GPa)	Proposed δ (nm)
Stafford <i>et al.</i> ⁴ , $114 \cdot 10^3$ g/mol PS [†]	4.2	0.1	2	3.81	0.0015 – 0.64	1.3 – 2.5
Stafford <i>et al.</i> ⁴ , $1800 \cdot 10^3$ g/mol PS [†]	4.2	0.1	2	4.18	0.002 – 0.62	1.1 – 2.2
Choi <i>et al.</i> ³ , Pt	130 – 180	n/a	n/a	169	0.0021 – 162.5	0.5 – 1.0
Tank <i>et al.</i> ⁵ , pentacene	16.09	n/a	n/a	5.9	$3 \cdot 10^{-7}$ – $8 \cdot 10^{-6}$	1 – 24

Table 2 In this table, we fit our quad-layer model to experimental data comparing t_f and λ_{cr} . The notation used in this table is illustrated in Fig. 4. There is good agreement between the value of E_f between our quad-layer model and the reported results in Stafford *et al.*. Notably, we report a range for δ and E_f^* because there is insufficient resolution when $t_f \approx \delta$ to assess these parameters independently. In Choi *et al.*, the objective is to verify the wrinkle-based approach for determining nano-scale thin film properties. We take their approach one step further by acknowledging that thin interfacial layers either at the free surface or at the film/substrate interface may be present. The average modulus computed in Choi *et al.* is 172 GPa, which is 2.4% different from the bulk modulus of Pt (168 GPa). Using our model, we compute a film modulus 0.59% different from the known bulk modulus, further demonstrating that in metrology of ultrathin films the consideration of interfacial layers may be important. In Tank *et al.*, it is noted that the modulus of pentacene was an order of magnitude higher than the modulus of other organic materials tested, and that the pentacene film was prone to buckling delamination due to poor adhesion on the PDMS substrate. For this reason, we approached the experimental data with our basic tri-layer model, which is ideally suited to scenarios with poor attachment between film and substrate (for this model, $t_i = \delta$ and $t_i = 0$). Using this approach, we computed an elastic modulus for pentacene significantly lower than the one reported in Tank *et al.*. [†] Plane strain modulus reported for consistency with original.

are effectively negligible for films not classified as ultrathin. In Stafford *et al.*, this deviation from typical behavior is addressed by treating the film layer as a composite of bulk material, with plane strain modulus E_f , and surface region with thickness δ and modulus E_f^* . This model is explained in detail in Sec. 2.2. For the remainder of this section, we use the notation in Stafford *et al.*, illustrated in Fig. 4.

In Fig. 4 the difference between our quad-layer model, the traditional bi-layer model that does not have an interfacial regions,

and the Stafford model is illustrated for both λ_{cr} and ϵ_{cr} . With regard to ϵ_{cr} , the strain required for an instability to appear, this figure clearly indicates that at sufficiently high strains films with thickness less than δ can still experience the wrinkling instability. Figure 4 also shows the influence of selected values of E_f^* on system behavior, notably for $E_f^* < E_f$ the difference in selection is only apparent in the region where $t_f \approx \delta$. This observation is relevant in fitting these models to experimental data, because the parameters E_f , E_f^* and δ must all be selected. Notably, there is a

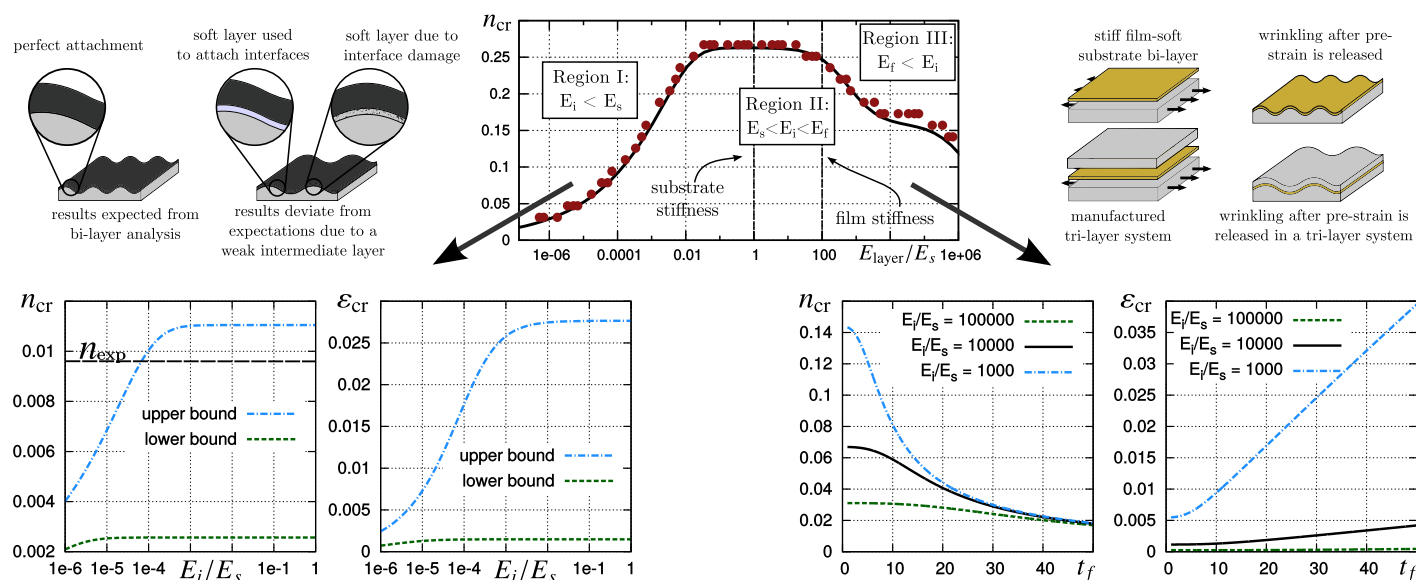


Fig. 5 This figure illustrates the applications of our model beyond buckling based metrology. The central plot shows three distinct regions of our model with respect to different values of E_i . In this plot, region I corresponds to $E_i < E_s$, region II corresponds to $E_s < E_i < E_f$ and region III corresponds to $E_f < E_i$. To the left, a weak or damaged interfacial layer potentially causing change in global system behavior is illustrated. The accompanying plots show parameters specific to the experimental system reported in Xie *et al.*⁸. Consistent with the parameters presented in Table 3, n_{cr} is reported in nm^{-1} . As illustrated in the left most plot, the observed value of n_{cr} , $0.0097 nm^{-1}$ is within the bounds of our model at the damage levels we anticipate. The plot of ϵ_{cr} indicates that the lower and upper bounds of ϵ_{cr} are below the maximum possible critical strain $\epsilon_{cr} = 0.03$ (see Table 3 for more information). To the right, an illustration for applications in studying new systems shows an embedded thin film. The accompanying graphs show how our model can be used to measure instability behavior of embedded thin films both for n_{cr} and ϵ_{cr} . In these plots, the length scale is defined by the thickness of the film and intermediate layer. For this example, we vary t_f (nm), hold $t_i = 1.0 nm$ and keep E_f and E_s identical similar to the graphic. The resulting value of λ_{cr} is reported in nm .

challenge associated with selecting these values because E_f^* and δ cannot be selected independently without sufficient information about behavior at film thicknesses approaching or less than δ . In both our proposed model and the Stafford model, it is apparent that a more realistic approach to fitting the data acknowledges that identical contribution of the additional layers to film stiffness when $t_f > \delta$ can be achieved with multiple combinations of E_f^* and δ . With this in mind, we provide a range of reasonable estimates for E_f^* and δ in fitting our model to experimental data. Table 2 shows a comparison between our quad-layer model for buckling based metrology of ultrathin films and other experiments and model fittings available in the literature.

The main outcomes of applying our model to buckling based metrology of ultrathin films is an improved ability to capture the influence of additional interfacial layers. Our examples also highlight the need for a higher resolution of experimental data if E_f^* and δ must be computed with a higher level of accuracy, or if it is important to know if the interfacial layers are primarily on the top or bottom of the film. However, we also show that even when this information is not available E_f itself can be determined readily by fitting multiple data points to the model. In the case of an interfacial layer with finite thickness and modulus lower than that of the substrate, as may be the case when there is interfacial damage or a soft glue, our model is also well equipped to capture this by considering subsequent contribution to substrate stiffness.

3.2 Applications in novel engineering systems

In the buckling based metrology application of our model, the primary focus is on the region where intermediate layer stiffness lies between the stiffness of the film and the stiffness of the substrate. When the stiffness of the intermediate layer is less than the stiffness of the substrate, the intermediate layer will lower the total substrate stiffness felt by the film, as illustrated in Fig. 5. Beyond relevance to specifically inserted weak layers, this has relevance to interfacial layers with uniform damage across the interface, where full damage would correspond to an interfacial traction free flaw and a buckling delamination instability. We specifically explore this region where interfacial stiffness represents a damaged interface by examining a system of carbon nanotubes (CNTs) adhered to a compliant substrate. This novel engineered system uses CNTs to access the nanoscale and global instability behavior to access the mesoscale (10 – 100s nm) to form a bio-interface, a surface with topological features on the same length scale as biological cells.⁶ This system in Xie *et al.*⁶ is notable because in contrast to the system in Yu *et al.*,⁶⁸ where a CNT film exhibits typical wrinkling behavior after being applied to a substrate while the substrate is prestrained, compression arises in the film due to the swelling/shrinking procedure illustrated in Fig. 6 and produces a film morphology not fully explained by wrinkling. In top view, the morphology resembles other systems with either uniaxial or multi-directional compression depending on the location within the film,^{69–72} however, the high ratio between peak amplitude and width of the wrinkles in profile indicates that the film and substrate separate at some locations, despite remaining glob-

ally attached.⁶ Mechanistically, this different morphology can be explained by recognizing that the CNT film is bonded to the PU substrate by weak van der Waals forces, which can be overcome by film-substrate separation. A damaged interfacial layer will facilitate film-substrate separation, and therefore detachment, at locations of peak amplitude.

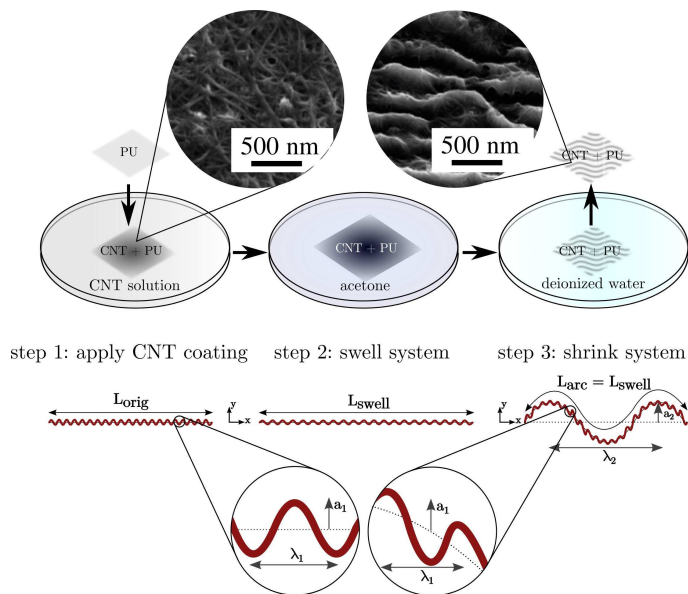


Fig. 6 This figure shows a typical example of a procedure to induce compression in a thin stiff film adhered to a compliant substrate. Shown is the three step bio-interface fabrication process used in Xie *et al.*⁶ In the first step, surface coating, the carbon nanotubes (CNTs) are attached to the surface of a polyurethane (PU) sponge that has been treated with oxygen plasma to enhance attachment. In the second step, the entire system is soaked in an acetone solution which causes the system to swell and the CNT film to deform irreversibly. Third, the entire system is soaked in deionized water which causes it to shrink back to the original configuration. In the third step, the substrate returns to a stress free configuration, while the irreversible film deformation in step two causes compression and out of plane buckling to arise in the film.⁶ The SEM images of the CNT film before and after swelling show the wavy surface topology created by this treatment. The surface profile schematic during each step of fabrication is used to approximate values in Table 3. The values a_1 and λ_1 are preserved from the first to final phase while a_2 is zero until the final phase. The parameter λ_2 is fitted to relate R and S .

The difference in fabrication process between Yu *et al.*⁶⁸ and Xie *et al.*⁶ suggests that applying the film prior to substrate stretching is the key to realizing this alternative outcome. During the swelling procedure, the CNT film will deform irreversibly, and will not necessarily form new attachments with the substrate below it. Therefore, an upper bound for level of interfacial damage would be related to the amount of swelling due to the exposure of new substrate surface at the interface. In addition, there is evidence of a small amount of slippage in individual CNTs deposited on prestrained films,⁷⁴ which indicates that even if the film fully forms new connections during swelling there will most likely be a small amount of interfacial damage due to slippage. The quantitative implications of this are summarized in Table 3. To capture the damaged interfacial layer, we frame the problem using our

	Method	Value
t_f	Computed by first approximating the surface profile as a sum of nanoscale and mesoscale features, $y = a_1 \sin(\frac{\lambda_1}{2\pi}x) + a_2 \sin(\frac{\lambda_2}{2\pi}x)$, with a_1 , a_2 , λ_1 , λ_2 , as the nano and mesoscale amplitude and wavelength respectively (illustrated in Fig. 6), and then relating amplitude and roughness (R), $R^2 = \frac{1}{n} \sum_{i=1}^n y_i^2 = \frac{\int_0^\infty [a_1 \sin(\frac{\lambda_1}{2\pi}x) + a_2 \sin(\frac{\lambda_2}{2\pi}x)]^2 dx}{\int_0^\infty dx}$ and subsequently computing film thickness (t_f) from the roughness before any swelling has occurred (R_0), $t_f = \frac{\int_0^\infty [a_1 + a_1 \sin(\frac{\lambda_1}{2\pi}x)] dx}{\int_0^\infty dx} = a_1 = \sqrt{2}R_0.$	$\approx 30 \text{ nm}$
λ_{cr}	By relating roughness and swelling (S), $S = \frac{\int_0^{L_{orig}} \sqrt{1 + [\frac{\lambda_2}{2\pi} (\sqrt{2R^2 - a_1^2}) \cos(\frac{\lambda_2}{2\pi}x)]^2} dx}{L_{orig}},$ the value for λ_2 that fits the experimental data is λ_{cr} . This value is also sensible based on inspection of the experimental images.	$\approx 650 \text{ nm}$
ϵ_{cr}	Known to be under 0.03, because wrinkles appear at 3 % swelling. Reported values correspond to the range computed by the equations in Sec. 2.1 and the other parameters.	0.0015-0.028
E_s, ν_s	Kanyanta and Ivankovic ⁷³	$E_s = 1 - 10 \text{ MPa}$, $\nu_s = 0.5$
E_f, ν_f	Yu <i>et al.</i> ⁶⁸	$E_f = 1 - 8 \text{ GPa}$, $\nu_f = 0.3$
E_i	The interface experiences between 1% and 20% damage. The lower limit is based on Khang <i>et al.</i> ⁷⁴ where a small fraction of CNTs slipped on a soft substrate during stretching. The upper limit is based on considering that no additional CNTs attach to the substrate during maximum stretching. ⁶	$0.8E_s - 0.99E_s$
t_i	Calculated by assuming that the thickness of the intermediate layer is on the order of the thickness of a single CNT not prone to collapse. ⁷⁴⁻⁷⁶	$1 - 3 \text{ nm}$

Table 3 Parameters computed from the experimental data provided in Xie *et al.*⁶.

basic tri-layer model, as a system with three continuum layers: a substrate, an intermediate region dominated by substrate/CNT attachment, and a CNT film. Given this framework we approximate model parameters from experimental data and literature, as summarized in Table 3. From the Region I plot in Fig. 5, it is apparent that even when there is substantial interfacial damage (in this case up to 20%), the instability initiation remains similar to the bi-layer wrinkling solution. The plot in Fig. 5, created using the range of parameters provided in Table 3, indicates that describing the experimental system in Xie *et al.*⁶ using our basic tri-layer model is consistent with experimental results.

The third region illustrated in Fig. 5, where intermediate layer stiffness exceeds film stiffness, has potential relevance to emerging technology in stretchable electronics. At present, novel materials and configurations are used to create stretchable electronics that take advantage of buckling and wrinkling behavior.^{1,77,78} In future applications, one possible approach would be to integrate stiff conductive films into electronic devices by placing them on top of a soft substrate and embedding them underneath a soft layer of material with either identical or similar modulus to the substrate itself. In these systems, wrinkling behavior may be harnessed or suppressed by carefully controlling film thickness and/or substrate material properties. As illustrated in Fig. 5, and Sec. 2 our model readily predicts critical wrinkling wavelength and strain for these systems given geometry and material properties. Figure 3 illustrates numerical verification of our analytical solution for these systems both in critical strain and wavelength, and the same numerical procedure could be used to analyze systems with complex geometry that may violate the assumptions of the analytical solution. The combination of analytical and numerical methods is a remarkable tool for understanding the behavior of these systems.

4 Concluding remarks

In conclusion, we created a novel model to capture instability behavior in systems that contain multiple interfacial layers. We accomplish this by beginning with a traditional bi-layer model and extending it to account for an interfacial layer between the film and substrate and at the surface of the film for the full range of possible interfacial layer stiffness. The analytical solutions for critical strain and wavelength for our model are also verified by numerical results. After defining our model, we demonstrate the application of our model to buckling based metrology in ultrathin films and novel engineering systems. Moving forward, our investigation can be used to elucidates behavior of a systems that deviate from well understood bi-layer wrinkling due the presence of interfacial layers.

Acknowledgments

This material is based upon work supported by the National Science Foundation Graduate Research Fellowship under Grant No. DGE-114747.

References

- 1 D. Y. Khang, J. A. Rogers and H. H. Lee, *Advanced Functional Materials*, 2009, **19**, 1526–1536.
- 2 W. Xia and S. Keten, *Extreme Mechanics Letters*, 2015, **4**, 89–95.
- 3 H. J. Choi, J. H. Kim, H. J. Lee, S. A. Song, H. J. Lee, J. H. Han and M. W. Moon, *Experimental Mechanics*, 2010, **50**, 635–641.
- 4 C. M. Stafford, B. D. Vogt, C. Harrison, D. Julthongpipit and R. Huang, *Macromolecules*, 2006, **39**, 5095–5099.
- 5 D. Tank, H. H. Lee and D. Y. Khang, *Macromolecules*, 2009, **42**, 7079–7083.
- 6 X. Xie, W. Zhao, H. R. Lee, C. Liu, M. Ye, W. Xie, B. Cui, C. S. Criddle and Y. Cui, *ACS Nano*, 2014, 11958–11965.
- 7 A. Goriely and M. Ben Amar, *Physical Review Letters*, 2005, **94**, 1–4.
- 8 T. R. Hendricks and I. Lee, *Nano Letters*, 2007, **7**, 372–379.
- 9 Q. Wang and X. Zhao, *Scientific Reports*, 2015, **5**, 8887.
- 10 H. Mei, R. Huang, J. Y. Chung, C. M. Stafford and H. H. Yu, *Applied Physics Letters*, 2007, **90**, 1–4.
- 11 M.A.Biot, *Journal of Applied Mathematics and Mechanics*, 1937, **22**, 984–988.
- 12 A. L. Volynskii, S. Bazhenov, O. V. Lebedeva and N. F. Bakeev, *Journal of Materials Science*, 2000, **35**, 547–554.
- 13 A. Evans and J. Hutchinson, *International Journal of Solids and Structures*, 1984, **20**, 455–466.
- 14 N. Bowden, S. Brittain and A. Evans, *Nature*, 1998, **393**, 146–149.
- 15 C. J. Brennan, J. Nguyen, E. T. Yu and N. Lu, *Advanced Materials Interfaces*, 2015, n/a–n/a.
- 16 S. Budday, P. Steinmann and E. Kuhl, *Journal of the Mechanics and Physics of Solids*, 2014, **72**, 75–92.
- 17 J. Dumais, *Current Opinion in Plant Biology*, 2007, **10**, 58–62.
- 18 M. Kücken, *Forensic Science International*, 2007, **171**, 85–96.
- 19 X. Lu and Y. Xia, *Nature Nanotechnology*, 2006, **1**, 163–164.
- 20 J. A. Rogers, T. Someya and Y. Huang, *Science*, 2010, **327**, 1603–1607.
- 21 D. Y. Khang, J. A. Rogers and H. H. Lee, *Advanced Functional Materials*, 2009, **19**, 1526–1536.
- 22 C. M. Stafford, C. Harrison, K. L. Beers, A. Karim, E. J. Amis, M. R. VanLandingham, H.-C. Kim, W. Volksen, R. D. Miller and E. E. Simonyi, *Nature Materials*, 2004, **3**, 545–550.
- 23 F. Greco, T. Fujie, L. Ricotti, S. Taccola, B. Mazzolai and V. Mattoli, *ACS Applied Materials and Interfaces*, 2013, **5**, 573–584.
- 24 M. Leser, J. Pegan, M. El Makkaoui, J. C. Schlatterer, M. Khine, M. Law and M. Brenowitz, *Lab Chip*, 2015, **15**, 1381–1388.
- 25 M. Ortiz and G. Gioia, *Journal of the Mechanics and Physics of Solids*, 1994, **42**, 531–559.
- 26 J. D. Whitcomb, *Composites Science and Technology*, 1986, **25**, 19–48.
- 27 C. Linder and A. Raina, *Computer Methods in Applied Mechanics and Engineering*, 2013, **253**, 558–583.

- 28 C. Linder and X. Zhang, *International Journal for Numerical Methods in Engineering*, 2013, **96**, 339–372.
- 29 C. Linder and X. Zhang, *Computer Methods in Applied Mechanics and Engineering*, 2014, **273**, 143–160.
- 30 A. Raina and C. Linder, *International Journal of Solids and Structures*, 2015, **75-76**, 247–259.
- 31 S. Tarasovs and J. Andersons, *Microelectronics Reliability*, 2012, **52**, 296–299.
- 32 M. D. Thouless, *IBM Journal of Research and Development*, 1994, **38**, 367–377.
- 33 D. Vella, J. Bico, A. Boudaoud, B. Roman and P. M. Reis, *Proceedings of the National Academy of Sciences of the United States of America*, 2009, **106**, 10901–10906.
- 34 A. A. Volinsky, N. R. Moody and W. W. Gerberich, *Acta Materialia*, 2002, **50**, 441–466.
- 35 V. M. Pereira, A. H. Castro Neto, H. Y. Liang and L. Mahadevan, *Physical Review Letters*, 2010, **105**, 1–4.
- 36 S. F. Ahmed, G.-H. Rho, K.-R. Lee, A. Vaziri and M.-W. Moon, *Soft Matter*, 2010, **6**, 5709.
- 37 P. Müller and J. Kierfeld, *Physical Review Letters*, 2014, **112**, 1–5.
- 38 H. S. Park, Q. Wang, X. Zhao and P. A. Klein, *Computer Methods in Applied Mechanics and Engineering*, 2013, **260**, 40–49.
- 39 F. Brau, H. Vandeparre, A. Sabbah, C. Poulard, A. Boudaoud and P. Damman, *Nature Physics*, 2010, **7**, 56–60.
- 40 Z. Huang, W. Hong and Z. Suo, *Physical Review E*, 2004, **70**, 3–6.
- 41 Z. Y. Huang, W. Hong and Z. Suo, *Journal of the Mechanics and Physics of Solids*, 2005, **53**, 2101–2118.
- 42 T. J. W. Wagner and D. Vella, *Physical Review Letters*, 2011, **107**, 1–4.
- 43 F. Jia, Y.-P. Cao, T.-S. Liu, Y. Jiang, X.-Q. Feng and S.-W. Yu, *Philosophical Magazine*, 2012, **92**, 1554–1568.
- 44 C. Lu, I. Dönch, M. Nolte and A. Fery, *Chemistry of Materials*, 2006, **18**, 6204–6210.
- 45 A. J. Nolte, R. E. Cohen and M. F. Rubner, *Macromolecules*, 2006, **39**, 4841–4847.
- 46 F. Jia, Y.-P. Cao, T.-S. Liu, Y. Jiang, X.-Q. Feng and S.-W. Yu, *Philosophical Magazine*, 2012, **92**, 1554–1568.
- 47 H. G. Allen, *Analysis and Design of Structural Sandwich Panels: The Commonwealth and International Library: Structures and Solid Body Mechanics Division*, Elsevier, 2013.
- 48 R. Huang, *Journal of the Mechanics and Physics of Solids*, 2005, **53**, 63–89.
- 49 S. Bédahy, P. Lipnik, T. Pardoën, C. Nascimento, B. Patris, P. Bertrand and S. Yunus, *Langmuir*, 2010, **26**, 3372–3375.
- 50 W. T. S. Huck, N. Bowden, P. Onck, T. Pardoën, J. W. Hutchinson and G. M. Whitesides, *Langmuir*, 2000, **16**, 3497–3501.
- 51 B. Biassé, M. Bruel and M. Zussy, *Process for transferring a thin film from an initial substrate onto a final substrate*, 1999.
- 52 A. Javili, B. Dortdivanlioglu, E. Kuhl and C. Linder, *Computational Mechanics*, 2015, **56**, 405–420.
- 53 J. Y. Chung, A. J. Nolte and C. M. Stafford, *Advanced Materials*, 2011, **23**, 349–368.
- 54 Y. Mei, S. Kiravittaya, S. Harazim and O. G. Schmidt, *Materials Science and Engineering R: Reports*, 2010, **70**, 209–224.
- 55 A. J. Nolte, M. F. Rubner and R. E. Cohen, *Society*, 2005, 5367–5370.
- 56 F. Greco, A. Bellacicca, M. Gemmi, V. Cappello, V. Mattoli and P. Milani, *ACS Applied Materials & Interfaces*, 2015, 7060–7065.
- 57 R. Huang, C. Stafford and B. Vogt, *Journal of Aerospace Engineering*, 2007, **20**, 38–44.
- 58 J. M. Torres, N. Bakken, C. M. Stafford, J. Li and B. D. Vogt, *Soft Matter*, 2010, **6**, 5783.
- 59 J. M. Torres, C. M. Stafford and B. D. Vogt, *ACS Nano*, 2010, **4**, 5357–5365.
- 60 J. M. Torres, C. M. Stafford and B. D. Vogt, *Polymer*, 2010, **51**, 4211–4217.
- 61 J. M. Torres, C. M. Stafford and B. D. Vogt, *ACS Nano*, 2009, **3**, 2677–2685.
- 62 K. Mansfield and D. Theodorou, *Macromolecules*, 1991, **24**, 6283–6294.
- 63 T. B. Karim and G. B. McKenna, *Polymer*, 2011, **52**, 6134–6145.
- 64 K. Miyake, N. Satomi and S. Sasaki, *Applied Physics Letters*, 2006, **89**, 20–23.
- 65 N. Bowden, W. T. S. Huck, K. E. Paul and G. M. Whitesides, *Applied Physics Letters*, 1999, **75**, 2557.
- 66 K. Efimenko, W. E. Wallace and J. Genzer, *Journal of colloid and interface science*, 2002, **254**, 306–315.
- 67 C. C. Fu, A. Grimes, M. Long, C. G. L. Ferri, B. D. Rich, S. Ghosh, S. Ghosh, L. P. Lee, A. Gopinathan and M. Khine, *Advanced Materials*, 2009, **21**, 4472–4476.
- 68 C. Yu, C. Masarapu, J. Rong, B. Wei and H. Jiang, *Advanced Materials*, 2009, **21**, 4793–4797.
- 69 D. B. H. Chua, H. T. Ng and S. F. Y. Li, *Applied Physics Letters*, 2000, **76**, 721.
- 70 J. Groenewold, *Physica A: Statistical Mechanics and its Applications*, 2001, **298**, 32–45.
- 71 L. He, C. Tang, X. Xu, P. Jiang, W.-M. Lau, F. Chen and Q. Fu, *Surface and Coatings Technology*, 2015, **261**, 311–317.
- 72 S. Yang, K. Khare and P. C. Lin, *Advanced Functional Materials*, 2010, **20**, 2550–2564.
- 73 V. Kanyanta and A. Ivankovic, *Journal of the Mechanical Behavior of Biomedical Materials*, 2010, **3**, 51–62.
- 74 D. Y. Khang, J. Xiao, C. Kocabas, S. MacLaren, T. Banks, H. Jiang, Y. Y. Huang and J. A. Rogers, *Nano Letters*, 2008, **8**, 124–130.
- 75 H. Maune and M. Bockrath, *Applied Physics Letters*, 2006, **89**, 173131.
- 76 A. N. Volkov and L. V. Zhigilei, *ACS Nano*, 2010, **4**, 6187–6195.
- 77 D. H. Kim, Y. S. Kim, J. Wu, Z. Liu, J. Song, H. S. Kim, Y. Y. Huang, K. C. Hwang and J. A. Rogers, *Advanced Materials*, 2009, **21**, 3703–3707.
- 78 S. P. Lacour, S. Wagner, Z. Huang and Z. Suo, *Applied Physics Letters*, 2003, **82**, 2404–2406.